Hole-Drilling Residual Stress Measurement with Artifact Correction Using Full-Field DIC

G.S. Schajer · B. Winiarski · P.J. Withers

Abstract A full-field, multi-axial computation technique is described for determining residual stresses using the hole-drilling method with DIC. The computational method takes advantage of the large quantity of data available from full-field images to ameliorate the effect of modest deformation sensitivity of DIC measurements. It also provides uniform residual stress sensitivity in all in-plane directions and accounts for artifacts that commonly occur within experimental measurements. These artifacts include image shift, stretch and shear. The calculation method uses a large fraction of the pixels available within the measured images and requires minimal human guidance in its operation. The method is demonstrated using measurements where residual stresses are made on a microscopic scale with hole drilling done using a Focused Ion Beam – Scanning Electron Microscope (FIB-SEM). This is a very challenging application because SEM images are subject to fluctuations that can introduce large artifacts when using DIC. Several series of measurements are described to illustrate the operation and effectiveness of the proposed residual stress computation technique.

G.S. Schajer (✉)
Dept. Mechanical Engineering, University of British Columbia,
Vancouver V6T 1Z4, Canada
e-mail: schajer@mech.ubc.ca

B. Winiarski · P.J. Withers
School of Materials, University of Manchester,
Manchester M1 7HS, UK

Introduction

The hole-drilling method is a well-established and reliable technique for measuring residual stress in a wide range of materials. It involves drilling a small hole in the specimen, measuring the deformations of the surrounding surface, and evaluating the local residual stresses from the measured deformations [1, 2]. Traditionally, the surface deformations are made using strain gauges [3, 4], but in recent years optical methods such as ESPI [5, 6], Moiré [7, 8], and DIC [9–13] have been applied. Motivations for the use of optical methods include that they avoid the time-consuming attachment and wiring of strain gauges and that they enable a wide range of hole sizes to be used.

Early residual stress evaluations from optical data used methods based on the techniques used for strain gauge measurements [5, 10, 11, 14, 15]. However, this approach limits the data usage to a small subset of the total available from the full-field optical data. Different strategies can be followed to choose the data used, but they too involve only a small subset of the available data and typically require substantial human guidance to make the data selection.

A significant challenge when using full-field optical measurements is that the displacements to be measured are small relative to the resolution limit of the measurement methods, and thus the signal-to-noise ratio of the data is often quite modest. However, this effect can be offset by taking advantage of the large quantity of data available from the full-field optical measurements.

This paper explores the use of full-field data analysis techniques to exploit the great information richness available from optical images. The objective is to make the calculations as automated as possible and to minimize the need for human interaction. Techniques of this kind have been developed and successfully applied to ESPI measurements [6, 12, 16]. Here this approach is extended to DIC measurements and further developed. The DIC method has the advantage over the ESPI and Moiré methods that it gives displacements in multiple directions, in two dimensions with reasonable ease, and in three dimensions with more effort. This multi-directionality gives isotropic residual stress measurement sensitivity. In addition, the DIC method can be used over a wide range of length scales spanning several orders of magnitude from microns to meters [9, 17]. By comparison, ESPI and Moiré are typically useful for holes only in the millimeter range. DIC can resolve displacements of about 0.02 of a pixel width in optical camera images [22, 23] and about 0.05–0.15 of a pixel width in SEM images. In comparison, typical surface displacements caused by hole drilling are in the range 0.1–0.3 pixels. Thus, it is challenging to use DIC for hole drilling measurements because the technique has barely sufficient sensitivity to identify the small displacements that occur. In addition, the measurements are often prone to artifacts that can be much larger than the displacements of interest. However, the substantial redundancy that exists within the large quantity of data available from full-field DIC measurements provides opportunities for data averaging, error checking and elimination of systematic artifacts. The resulting approaches greatly reduce the effects both of random and systematic measurement errors. They enhance the accuracy and reliability of the measurements and substantially mitigate measurement concerns. An example application is considered here of Focused Ion Beam (FIB) hole-drilling residual stress measurements within a Scanning Electron Microscope (SEM). This is a particularly demanding application because SEM measurements are much less stable than conventional optical measurements, and are prone to much larger and more serious artifacts. These artifacts include image displacement, image stretching and image shear. Automatic techniques are developed here to identify and compensate for these artifacts and are shown to be effective. Because of the scale-independent character of DIC measurements, the methods developed are also useful for conventional macro-scale measurements and significantly enhance residual stress evaluation accuracy.

Full-Field Residual Stress Computation

In contrast to the traditional strain gauge style measurements, all optical techniques indicate surface displacements, not strain. Estimation of surface strains from displacement measurements involves numerical differentiation, which is an inherently noisy process, and so is to be avoided. Thus, it is desirable to work directly with displacement data.

The radial displacements of the surface around a circular hole drilled in a uniformly stressed material with dimensions much greater than the hole size have a trigonometric form [16]:

$$\delta_r(r,\theta)/a = [P\, u_r(r) + Q\, v_r(r)\cos 2\theta + T\, v_r(r)\sin 2\theta]/E \quad (1)$$

where the stress quantities

$$P = (\sigma_x + \sigma_y)/2, \quad Q = (\sigma_x - \sigma_y)/2, \quad T = \tau_{xy} \quad (2)$$

respectively represent the isotropic stress, the 45° shear stress, and the axial shear stress. In equation (1), $u_r(r,\theta)$ is the radial profile of the radial displacements caused by a unit isotropic stress P, and $v_r(r,\theta)$ is the radial profile of the radial displacements caused by unit shear stresses Q or T. The normalizations by hole radius a and Young's modulus E non-dimensionalizes the radial displacement profiles $u_r(r)$ and $v_r(r)$. The resulting numerical values depend on hole depth and can be computed using finite element analysis [16]. Since DIC measurements are scale independent, it is convenient to measure the displacements $\delta_r(r,\theta)$ and hole radius a in units of image pixels.

The corresponding circumferential displacements are:

$$\delta_\theta(r,\theta)/a = [Q\, v_\theta(r)\cos 2\theta + T\, v_\theta(r)\sin 2\theta]/E \quad (3)$$

A "P" term is absent in equation (3) because an isotropic stress causes only axi-symmetric displacements, in which case all circumferential displacements are identically zero. A relationship similar to equation (1) applies for the axial displacements $\delta_z(r,\theta)$, but is not required here because the present example focuses on 2-dimensional measurements. However, if 3-dimensional measurements were made, the data from the additional dimension could be directly incorporated into the calculations by extending the procedure described here.

In addition to the surface displacements due to hole drilling described in equations (1)–(3), surface displacements artifacts are also observed due to relative motion, axial magnification change and shearing of the imaging device. These artifacts can typically be controlled well when imaging using conventional cameras, but less effectively when imaging using a device such as a Scanning Electron Microscope [18]. Such artifacts are small and are not of concern in typical microscopy applications. However, even with modern SEM equipment, they become visible and very significant when using DIC to identify the very small surface displacements from hole drilling.

Relative motion, magnification change and shearing artifacts are systematic in character and thus can be identified and taken into account within the residual stress calculation. Equations (1) and (3) can be augmented to include these quantities. Rearranging the relationships into Cartesian coordinates to fit the axial format typically used for DIC calculations gives:

$$\delta_x(r,\theta)/a = \tfrac{1}{2}(u_r(r)\cos\theta + v_r(r)\cos 2\theta\cos\theta - v_\theta(r)\cos 2\theta\sin\theta)w_1$$

$$+ \tfrac{1}{2}(u_r(r)\cos\theta - v_r(r)\cos 2\theta\cos\theta + v_\theta(r)\cos 2\theta\sin\theta)w_2$$

$$+ (v_r(r)\sin 2\theta\cos\theta - v_\theta(r)\sin 2\theta\sin\theta)w_3$$

$$+ w_4 + (x/H)w_5 + (y/H)w_6 \tag{4}$$

$$\delta_y(r,\theta)/a = \tfrac{1}{2}(u_r(r)\sin\theta + v_r(r)\cos 2\theta\sin\theta + v_\theta(r)\cos 2\theta\cos\theta)w_1$$

$$+ \tfrac{1}{2}(u_r(r)\sin\theta - v_r(r)\cos 2\theta\sin\theta - v_\theta(r)\cos 2\theta\cos\theta)w_2$$

$$+ (v_r(r)\sin 2\theta\sin\theta + v_\theta(r)\sin 2\theta\cos\theta)w_3$$

$$+ w_7 + (y/H)w_8 + (x/H)w_9 \tag{5}$$

where the normalized quantities w_i, schematically illustrated in Fig. 1, are:

w_1 x stress, σ_x / E
w_2 y stress, σ_y / E
w_3 xy shear stress, τ_{xy} / E
w_4 x image displacement / H
w_5 x image stretch / H
w_6 x image shear / H
w_7 y image displacement / H
w_8 y image stretch / H
w_9 y image shear / H

and where x and y are the horizontal and vertical pixel coordinates with origin at the hole center, and H is the image height in pixels. Conceptually, some of the w_i could be normalized by the image width W, but to keep a consistent scaling among variables, H is used throughout. The choice of H or W for the normalization is not significant as long as the chosen quantity is consistently used.
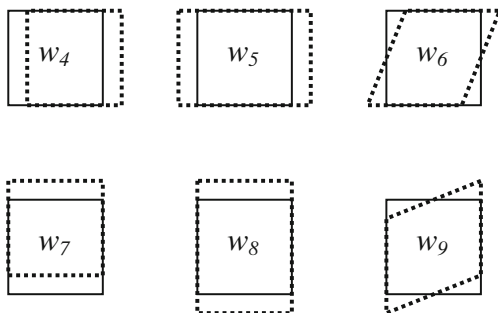

Fig. 1 Schematics of normalized deformation quantities w_i. w_4=x-displacement, w_5=x-stretch, w_6=x-shear, w_7=y-displacement, w_8=y-stretch, w_9=y-shear

The numbering system for the quantities w_i is used so that equations (4) and (5) can be expressed within a combined matrix equation. The normalizations are done so that the various quantities have similar sizes and so improve computational stability. A pair of equations (4) and (5) exists for each pixel selected from the image, typically some thousands of pixels. When expressed in matrix format, the resulting equation has the following structure [19], illustrated for the first six chosen pixels, with non-zero matrix coefficients indicated by asterisks.

$$\mathbf{G\,w} = \delta \tag{7}$$

Matrix $\mathbf{G}$ has $2N$ rows and 9 columns, where N is the number of pixels. Since N typically equals several hundreds of thousands, the number of rows (= number of data) greatly exceeds the number of columns (= number of quantities to be determined), and thus the matrix equation (7) is highly over-determined. A "best-fit" solution can be obtained by the least-squares method [20]. This can be conveniently computed by pre-multiplying both sides of equation (7) by the transpose of matrix $\mathbf{G}$. The resulting 9×9 matrix equation can be solved routinely.

$$\mathbf{G^T G\,w} = \mathbf{G^T}\delta \tag{8}$$

By paying attention to the sequence of the required multiplications, it is possible to form the 9×9 $\mathbf{G^T G}$ matrix and the 1×9 right-side vector $\mathbf{G^T}\delta$ by accumulating the various permutations of the products of the matrix coefficients and displacements at each pixel. This procedure minimizes the required numerical effort by avoiding the explicit creation and handling of the very large matrix $\mathbf{G}$ and right-side vector δ.

Theoretically, data from every pixel surrounding the hole could be accumulated into equation (6). However, data from the pixels very close to the hole edge are unreliable because the hole cutting process damages the surface imaged in this area. Data from pixels far away from the hole edge are also not useful because the displacements due to hole drilling become too small to contribute significantly to the stress calculation. Following previous practice for ESPI calculations, data are taken from pixels within an annular area surrounding the drilled hole [16]. For the SEM images considered here, an inner radius 1.7 times the hole radius was found to be the minimum sufficient to avoid the faulty data near the hole edge. Choice of outer radius is less critical; about twice the inner radius appears to provide a reasonable balance between far-field data to identify measurement artifacts and near-hole data to identify the residual stresses. Inner and outer calculation area radii of 1.7 and 3.4 times the hole radius were used for all calculations reported here. To provide the required image geometry, including surrounding space for patches and imperfect hole centralization, the SEM magnification was chosen to give a hole diameter approximately 20 % of the image height.

If 3-dimensional DIC were used, equation (6) would have a similar but larger structure with 3 N rows and 12 columns. Since the resulting equation would have greater data content, some improvement in residual stress evaluation accuracy can be anticipated. This improvement is likely to occur from the somewhat superior in-plane displacement evaluations provided by the 3-D DIC technique. However, the improvement due to the addition of the out-of plane displacements may be modest because these displacements are small compared with the in-plane displacements and their evaluation accuracy is relatively poor.

Taking the opposite approach, it is also possible to use 1-dimensional data, for example, x-displacements using only the upper half of the matrix in equation (6), or y-displacements using only the lower half of the matrix. Such calculations can give useful results. However, stresses in one direction produce displacements mainly in that direction, with much smaller displacements in the transverse direction. Thus, calculations using only x-displacements will give less reliable results for the y-stresses, and vice-versa for calculations using only y-displacements. A calculation using equation (6) with both displacement components together is spatially symmetrical and gives superior results for all stress components.

Digital Image Correlation

Digital Image Correlation is a well-established method for evaluating the surface displacements that have occurred between successive images of the surface of interest [21,

22]. Typically, DIC is used with optical images measured by digital cameras. In this study, an SEM is used to record the images. The 2-D DIC method used here involves comparing two successive images of the target surface, taken before and after hole drilling. The image correlation proceeds by selecting a local area of pixels, a "patch" within the first image, and then locating the corresponding patch position within the second image based on the position of maximum correlation. Interpolation techniques allow the relative position of corresponding patches to be determined to within 0.02 or less of a pixel spacing [22]. To allow flexibility in subsequent residual stress computations, a custom-written computer code was written for this calculation. For computational compactness and speed the DIC calculations were implemented using the correlation coefficient curve fitting method [23].

Patch size and shape are major factors that control DIC accuracy and resolution. Because the DIC evaluated displacements at a given point derive from data from a finite sized patch area around that point, there must be sufficient available image data around that point. Lack of available image data becomes an issue near to image boundaries and near the hole edge for hole-drilling images. Thus, DIC can only be used for image points beyond half a patch width from image boundaries. Small patches are therefore needed when DIC results are required close to image boundaries, notably near the edge of the drilled hole.

In general, increasing patch size improves correlation accuracy. However, since the data from a patch are aggregated to give an overall displacement vector, it is necessary that the pixels within the patch all have approximately similar displacements. Thus, large patches can only be used where displacement curvatures are small. Smaller patches must be used for images with sharply varying displacement fields. Some specialized DIC techniques can accommodate within-patch deformations [23] and so could allow the use of larger patches, but this possibility was not pursued here because in the most influential region near the hole boundary the patch size is constrained to be small.

The displacements to be identified for hole-drilling measurements are very small and so careful attention to patch size and shape is needed to maximize the quality of the DIC results. The square patches typically used for general-purpose DIC work are not ideally suited for use around the boundary of a circular hole because of their protruding corners. Thus, the width of the unavailable DIC evaluation area around the hole boundary enlarges in the ±45° areas. The use of circular instead of square patches eliminates this effect.

Since the region adjacent to the hole boundary contains the highest surface displacements, it is desirable to minimize the radius of the correlation patches used and thus the width of the unavailable boundary margin. Smaller correlation

patches are additionally appropriate near the hole boundary because the deformation gradients are relatively high. However, at locations further from the hole boundary, larger patches can be used because deformation gradients are lower and boundary proximity is not an issue. It is proposed here to use variable size patches, where the patch diameter is proportional to radial distance from the hole center. Thus, smaller patches are used near the hole boundary, and larger patches further away. A consequence of this strategy is that the DIC displacement uncertainty, which is inversely proportional to patch width [17], is non-uniform within the measured image. Fortunately, the higher uncertainty of the smaller patches near the hole boundary is compensated for by the larger local surface displacements.

A concern with the variable patch diameter strategy is that the patch size can get small in the data-rich region near the hole boundary. The limitation on patch size applies only in the direction perpendicular to the hole boundary; a patch can be larger in the parallel direction. Such circumferential enlargement is an acceptable possibility because the associated deformation gradients are smaller than those in the radial direction. Thus, it is chosen here to use elliptical patches with major axis oriented in the circumferential direction. Figure 2 shows an example SEM micrograph of a drilled hole with a selection of patches around it chosen with this strategy. (The number of patches shown in Fig. 2 is reduced and their distribution chosen so that their shape variation can be illustrated more clearly. In subsequent work, many more patches arranged in a rectangular grid are used.) The two largest concentric circles indicate the annular area containing the pixels at which DIC displacements are to be evaluated. The
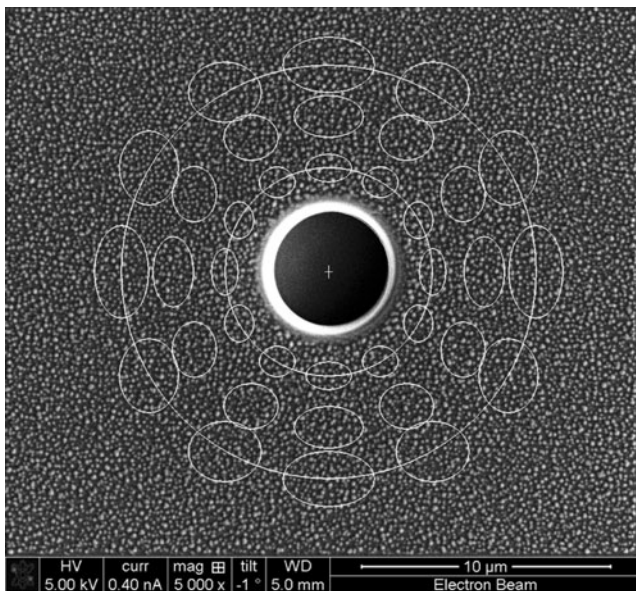
patches at the inner circle have shapes that successfully maintain a consistent margin from the surface distortions near the edge of the hole. The patch width increases linearly with distance from the hole, doubling at the outer annular circle. The combination of all these features significantly enhances the quality of the DIC results.

FIB-SEM Equipment

A dual beam FEI xT Nova NanoLab 600i FEGSEM/FIB microscope was used to sputter a pattern of nano Pt dots on the specimen surface. An FEI gas injection system and a standard molecular gas precursor for Pt deposition, $(CH_3)_3Pt$ $(CpCH_3)$, in the FIB-assisted deposition mode were used [17]. Before deposition, the sample was allowed to stabilise inside the vacuum chamber for more than 12 h. A pseudo-random nano Pt dot pattern was mapped onto the carbon-coated surface using the 1024×844 pixel bitmap shown in Fig. 2. This pattern, consisting of random black dots on a white background was prepared using Adobe Photoshop 7.0 software (Adobe Systems, Inc., USA) [17]. Prior to the hole-drilling experiments the surface of the beam was carbon coated (50 nm thick film) using a Gatan PECS 682 precise etching-coating system equipped with a Gatan 681.20000 Film Thickness Monitor, see [17] for details. This carbon coating eliminated surface charging effects on the amorphous Zr surface.

A series of micro-holes (typically approx. 5.0 μm in diameter and 2.4 μm deep) were FIB irradiated using 30 kV acceleration voltage and 0.92 nA beam current, taking 93 s to drill each hole. The precise dimensions were individually measured for each hole.

To achieve consistent and reliable SEM measurements for use with DIC, it is important to choose appropriate imaging conditions, namely working distance, voltage, current, dwell time, detection of secondary electrons (SE) or back-scattered electrons (BE), secondary ions (SI+), digital image resolution, etc. These were found following the recommendations in [17]. Thus each image of 1024×884 pixels suitable for DIC analysis was integrated from 8 e-beam scans (5 kV, 0.40 nA) with e-beam dwell time of 3 μs (total image acquisition time=21.7 s). Such acquired images yielded the lowest standard deviation of the DIC-indicated displacement within the image area and the effects of image shifts (the step changes in x- and y-direction) on the resulting displacement/strain field were negligible.

Fig. 2 Scanning electron micrograph of a drilled hole, showing example correlation patches of elliptical shape and variable size. (Many more patches are used for evaluating DIC displacement maps)

Experimental Measurements

Several series of measurements were conducted using the FIB-SEM equipment described in the previous section.

These measurements were designed to test and illustrate the features of the computation method and its ability to compensate for measurement artifacts. In addition, they were designed to investigate effective techniques for using FIB-SEM equipment to achieve the most reliable and stable measurements.

Hole-drilling residual stress measurements were made on a Zr-based bulk metallic glass specimen ($Zr_{50}Cu_{40}Al_{10}$ [24], E=95.0 MPa, ν=0.35) in the shape of a rectangular beam $16.4 \times 3.3 \times 1.05$ mm. The beam was cut with diamond cutting wheel using a Struers Acutom-5 precision cutting machine, polished with 600-, 1200- and 2500-grit paper, and then polished with ¼ micron diamond suspension. SEM images for DIC analyses were made before and after hole drilling using a FIB, as described in the previous section.

"Baseline" Measurements

The first series of measurements was designed to obtain SEM images with the smallest possible artifacts. The beam specimen was mounted within the FIB-SEM equipment and SEM images were taken immediately before and after using FIB to drill a set of five holes equally spaced along the specimen. Changes to equipment setup, e.g., magnification setting and vacuum maintenance, were minimized between SEM measurements. These measurements gave a baseline case for "good" measurements.

Figure 3(a) shows an example map of the x-displacements evaluated using DIC from the image shown in Fig. 2, using the variable-size elliptical correlation patches of the type shown in Fig. 2. The centers of these patches were chosen to form a rectangular grid at 15×15 pixel intervals and the displacements at the pixels throughout the image were linearly interpolated from the DIC estimated displacements at the grid pixels.

Figure 3 is presented in "fringe" format. This presentation format mimics the fringe patterns produced by ESPI measurements, where each fringe corresponds to a displacement of one wavelength. As such, Fig. 3 shows a topographical style map where the "contours" are the fringes, here spaced at intervals of 0.5 pixels. The more conventional choice of one pixel per fringe was halved to provide greater contrast when illustrating the small displacements in most images. Thus, in this presentation, the change from white to black corresponds to a displacement of 0.25 pixels. .

The largest displacements in Fig. 3(a) are approximately 0.2 of a pixel, which is a typical size for hole drilling in a high-E material (E=95.0 MPa here). This small displacement range places severe challenges on the measurement and computation methods. Great care must be taken to get as

Fig. 3 Example "baseline" x-displacement maps in "fringe" format, a transition from white to black corresponds to a 0.25 pixel displacement. (**a**) x-displacements, (**b**) x-displacements with artifacts subtracted, (**c**) ideal data corresponds to (**a**), (**d**) residuals = (**a**) – (**c**)
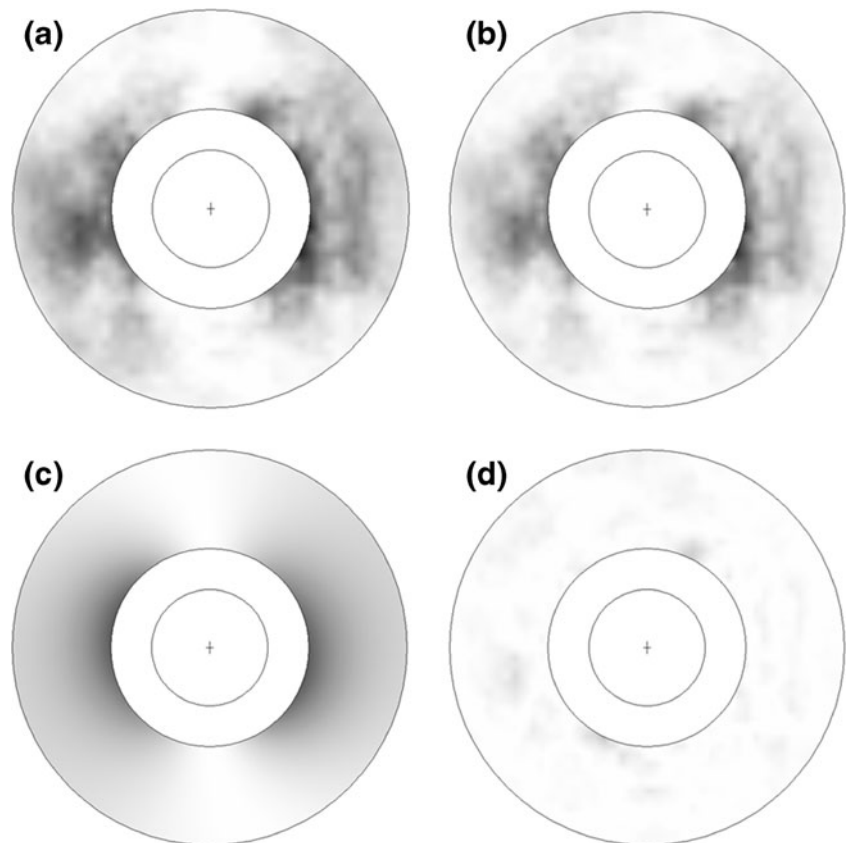
high quality data as possible, to do calculations that make most effective use of the available data and to use methods that are as immune as possible to measurement artifacts.

Table 1 shows the residual stresses computed from the DIC data in Fig. 3(a) using equation (7). The table also lists the calculated sizes of the computed displacement artifacts w_4 to w_9. The bulk displacements w_4 and w_7 evaluate as zero because the average x and y displacements within the annular computation area were previously subtracted from the DIC data. This preparatory step was done to centralize the fringe pattern in Fig. 3(a), but is otherwise not essential. Quantities w_5 and w_8 indicate the stretches in the x and y directions respectively, and w_6 and w_9 indicate the shears parallel to the x and y directions. In this well-controlled measurement, all these quantities are small.

The third row of Table 1 shows the residual stresses calculated using equation (7) with DIC data for both x and y displacements. As previously indicated, it is also possible to calculate residual stresses based on x or y displacements alone. In such cases, the computed stress that is in the same direction as the chosen displacements is computed more reliably than the perpendicular stress. The first three rows of Table 1 show that the residual stress calculation using dual axis displacements gives results that combine the single axis results, although not always giving a value between them. The dual axis results have a bias towards the more reliable of the single axis results, which certainly is a desirable property.

Returning to Fig. 3, map (b) shows the displacement data after the image stretching and shear corresponding to w_8 and w_9 have been subtracted. Since these artifacts are small in this example measurement, map (b) is very similar to map (a). Map (c) shows the ideal data that would be expected for the residual stresses and artifacts in map (a), calculated using the computed **w** values. This map should be a "clean" version of the actual measurements in map (a). The difference between the measured and ideal data is shown in the residuals map (d). If all goes well the residuals map should be close to null, with few if any significant features. The root-mean-square (rms) of the residual map (d) is about 0.03 pixels.

Measurements Including Artifacts

In a second series of measurements, SEM images were made after the instrument magnification was changed and then returned to its original setting and the vacuum chamber vented and then re-evacuated. Both of these actions, which occur when a sample needs to be removed between measurements, are known to make significant changes to the imaging conditions and thereby introduce measurement artifacts.

Figure 4 shows the displacement maps for an example measurement including very severe artifacts. This is for the same hole as Fig. 3, measured after magnification change, venting and re-evacuation. The numerous fringes visible in map (a) correspond to stretch and shear in the y direction. Each fringe represents one pixel displacement. For the x-displacements shown in Fig. 4, stretch and shear respectively create horizontal and vertical fringes (vice versa for x-displacements). These artifacts substantially dominate the displacements in Fig. 4(a). Figure 4(b) shows the displacement map after subtraction of the stretch and shear artifacts determined from the computed **w** values. This process is very effective, and the resulting map is very similar to Fig. 3(b). Likewise, the residuals map in Fig. 4(d) is also close to null, similar to Fig. 3(d). The computed stresses listed in the lower half of Table 1, corresponding to Fig. 4 are very similar to those in the upper half, corresponding to Fig. 3. These results clearly show the effectiveness of the artifact modeling in equation (7). A signal of maximum size 0.2 pixels has been successfully extracted from among artifacts creating apparent displacements of 7 pixels.

After some exploration, it was found that the source of the stretch artifact was hysteresis in the setting of the SEM magnification. A slightly different image magnification was produced when the magnification setting was made from a low to a high value than from a high to a low value. The difference is not large, less than 1 %, but even this change is enough to produce a shift of several pixels in an image that is 1024 pixels wide. The effect of this artifact was reduced to less than one pixel

Table 1 Residual stresses and measurement artifacts calculated using data from Figs. 2 and 3

Axis	x-stress MPa, from w_1	y-stress MPa, from w_2	shear MPa, from w_3	x-displ. pix/ H from w_4	x-stretch pix/ H from w_5	x-shear pix/ H from w_6	y-displ. pix/ H from w_7	y-stretch pix/ H from w_8	y-shear pix/ H from w_9
Fig. 3 x	−216	−225	6	0.00	−0.08	−0.04	-	-	-
Fig. 3 y	−191	−254	23	-	-	-	0.00	0.12	−0.01
Fig. 3 x & y	−219	−255	15	0.00	−0.08	−0.05	0.00	0.12	0.00
Fig. 4 x	−226	−301	9	0.00	4.65	5.16	-	-	-
Fig. 4 y	−223	−264	13	-	-	-	0.00	7.56	−3.53
Fig. 4 x & y	−219	−269	11	0.00	4.64	5.16	0.00	7.57	−3.53

Fig. 4 Example x-displacement maps with artifacts, each transition from white to black corresponds to a 0.25 pixel displacement. (a) x-displacements, (b) x-displacements with artifacts subtracted, (c) ideal data corresponds to (a), (d) residuals = (a) – (c)
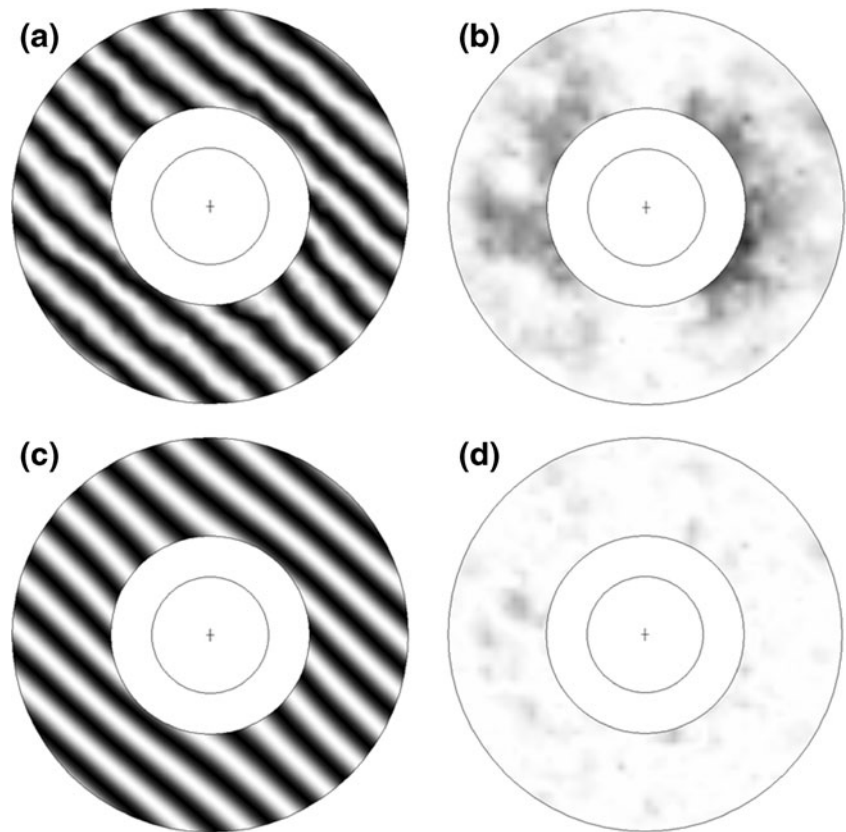
by ensuring that the last magnification change was always in the same direction, from low to high.

Measurements with Bending Load

In a third series of measurements, the beam specimen was centrally loaded within the three-point bending fixture shown in Fig. 5. SEM images were made on the beam specimen for a series of five equally spaced holes 50 μm apart, cut adjacent to the holes made during the first two series of measurements. New holes were cut so that the new total stresses (residual + applied) would be measured. This procedure was used so that the incremental effect of the applied loading could be identified by subtracting the residual stresses evaluated from the first series measurements from the third series measurements. This incremental approach was used to investigate hole-drilling residual stress evaluation accuracy because the initial residual stresses in the sample are not accurately known. Prior attempts to create stress-free samples were not successful because of the occurrence of recrystallization during the annealing process. The applied stresses induced in the beam sample were evaluated by measuring its upper surface shape using a Nanofocus μscan SC200 laser profilometer before and after loading.

Figure 6 shows a comparison of the hole-drilling measurements of the applied x-stresses created by the bending loading (third series measurements minus first series) with the stress values determined from the surface profile measurements. The equi-spaced arrangement of the holes on a uniform beam specimen gave the linear stress variation shown in the graph. Good agreement was achieved between the hole drilling measurements and theoretical expectations.
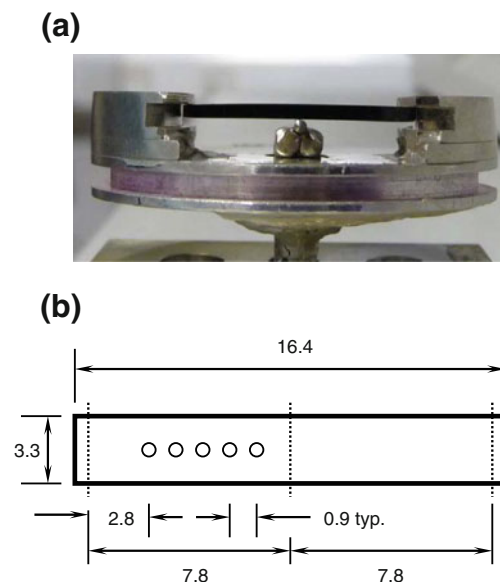

Fig. 5 Bending specimen, (a) specimen mounted in load frame, (b) specimen dimensions
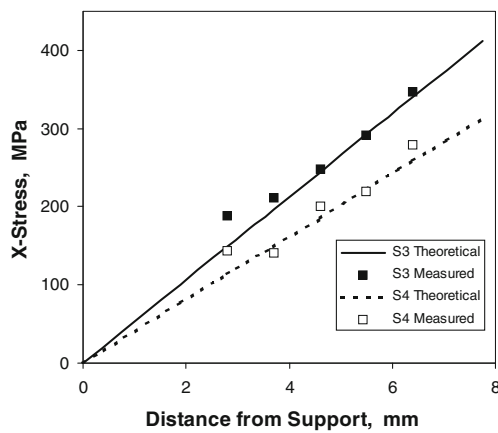
Fig. 6 Measured and theoretical stresses for the bend test specimen. "S3" = Series 3 tests (with "full" bending load), "S4" = Series 4 tests (with reduced bending load)

Measurements with a Reduced Bending Load

The above (third series) measurements were made under favourable conditions because both pre- and post- hole images were made with the loaded specimen kept in place within the SEM. A fourth series of measurements was conducted to evaluate the quality of measurements where the post-hole measurements were made after the specimen was removed, the bending load changed, and the specimen reloaded within the SEM. The existing holes cut during the third series measurements were then re-imaged. These measurements therefore included the adverse effects of magnification adjustment, vacuum chamber venting and specimen movement.

The lower line of Fig. 6 shows a comparison of the hole-drilling measurements of the applied x-stresses created by the bending loading (fourth series measurements minus first series) with the stress values determined from the surface profile measurements. Again, good agreement was achieved between the hole drilling measurements and theoretical expectations. The closeness of the agreement is remarkable because the need for very close angular alignment was not fully appreciated when the specimen was reloaded into the SEM. An angular error of about 0.3° occurred, enough to give a shift of several pixels across the height of the image, thereby producing a fringe pattern similar to Fig. 4(a). However, equation (7) was effective in compensating for

this error, and gave the stress results shown in Fig. 6. Subsequently, measurement procedures were adjusted to minimize the rotation error when reloading specimens. The adverse effects of the venting, specimen removal, replacement and the SEM re-evacuation can be seen by the increased scatter of the Series 4 points around the theoretical line in Fig. 6 compared with that of the Series 3 points.

Specimen Rotation Measurements

The occurrence of specimen rotation in the fourth series measurements prompted the addition of a short fifth series of measurements to investigate residual stress evaluation stability and angle estimation in the presence of known specimen rotations. SEM images were made on a single hole from the fourth series where the beam specimen was rotated ±0.1° using a precision rotary stage mounted within the SEM.

Table 2 lists the residual stresses and the artifacts computed from the images taken at the three angular positions. The computed residual stresses remain very stable and the shear values follow the expected trends very closely. A rigid-body rotation is represented mathematically as the combination of equal and opposite axial shears, 0.1° corresponding to $943 \times \pi \times 0.1 / 180 = \pm 1.65$ pixels in images 943 pixels high. The shear differences evaluated from the images closely reproduced this value. All these results demonstrated the effective functioning of the residual stress computation and artifact correction method.

Discussion

Residual stress evaluations from DIC data are challenging because the displacements created by hole drilling are small in the high-E materials of common interest, typically 0.1–0.3 pixels. This modest displacement sensitivity of DIC is just sufficient under ideal conditions, but causes a tendency to be affected by serious artifacts in non-ideal cases. The effectiveness of the proposed full-field residual stresses calculation method is demonstrated using measurements with a FIB-SEM. This is a very challenging application because images produced by a SEM are subject to small but very significant fluctuations. The fact that useful DIC-

Table 2 Computed residual stresses and artifacts for a specimen rotated by ±0.1°

Angle degrees	x-stress MPa	y-stress MPa	shear MPa	x-stretch pix/H	y-stretch pix/H	x-shear pix/H	y-shear pix/H	Δx-shear pix/H	Δy-shear pix/H
−0.1	49	−196	−10	−7.68	−7.05	−6.20	−0.47	-	-
0.0	19	−196	−3	−7.66	−7.03	−4.59	−2.12	1.61	−1.65
0.1	21	−193	−8	−7.69	−6.99	−2.98	−3.76	1.61	1.64

based residual stress evaluations are even possible is a testament to the high quality and stability of modern SEM imaging.

The local fluctuations in the DIC images can be seen by comparing the measured and ideal fringes shown Figs. 3 and 4, panels (b) and (d). The noise, with an rms about 0.12 pixels, is large compared with the stress-induced displacement of up to 0.3 pixels. It is also large compared with optical measurements made using a digital camera (typical rms=0.02 pixels [22]). This lesser performance occurs here because a SEM is a scanning instrument for which small electrical fluctuations cause corresponding small fluctuations in the geometrical positions of the pixels in successive scans. These sub-pixel fluctuations don't disturb the intended microscopy purpose of an SEM but are serious for DIC work. In comparison, a digital camera has superior DIC performance because its pixels are rigidly laid out on the detector surface.

The low signal-to-noise ratio of DIC can significantly impair residual stress evaluation accuracy, even when using the proposed full-field method with artifact correction. Based on observation of the variation of the computed residual stresses in Fig. 6, the standard error is estimated to be about 50 MPa for the present FIB-SEM measurements. An additional source of error specific to FIB-SEM measurements is the possible introduction of localized residual stresses due to the FIB hole drilling. The size of this possible stress introduction could not be evaluated here because the measurements reported in Fig. 6 are all differential in character.

Conventional hole drilling residual stress measurements on the macro-scale using optical measurements of holes mm or larger in diameter are much less prone to measurement artifacts. However, they retain the same low displacement sensitivity as FIB-SEM measurements and thus can benefit from the use of the full-field computation method presented here. Useful residual stress evaluation results were achieved by Nelson [10] when using 16 selected points within the measured images; certainly much greater computational stability can be expected when using data from several hundred thousand pixels with automated artifact correction. The full-image data usage also removes any need for human selection of the particular data to be used for the residual stress calculation. The time required to complete the full-field calculations is small compared with the measurement time, about 20 s on an ordinary laptop (Intel Atom 1 GHz, 1 GB of RAM) computer for the DIC, and about 3 s for the stress evaluation.

The results presented here are for the case where the residual stress is uniform within the hole depth. This is closely approximated in the example presented here for bending loading and a hole depth a tiny fraction of the beam depth. Residual stresses that vary with depth can be evaluated using the Integral Method [1], and good results should be achieved when using camera-based optical measurements. More modest performance is likely when using SEM measurements because of the associated variabilities associated with the scanning process.

Conclusions

A full-field computation technique is described and successfully demonstrated for determining residual stresses using the hole-drilling method with DIC. The computational method exploits the large quantity of data available from optical images to ameliorate the effect of modest deformation sensitivity of DIC measurements and requires minimal human guidance in its operation. In addition, the substantial data redundancy allows for commonly occurring measurement artifacts such as image shift, stretch and shear to be accounted for and their effects mathematically eliminated. Other systematic artifacts could similarly be accounted for and eliminated. The multi-axial deformation measurement capability of DIC is also exploited to provide further data and also to enable uniform residual stress sensitivity in all in-plane directions.

The proposed method is demonstrated using measurements where residual stresses are made on a microscopic scale within a Scanning Electron Microscope with hole drilling done using a Focused Ion Beam. This is a very demanding application because SEM images are subject to fluctuations that can introduce large artifacts when using DIC. By comparison, conventional optical measurements using a digital camera and much more stable, so a computational method that works with SEM data should certainly work well with optical data. Several series of measurements are described to illustrate the operation and effectiveness of the proposed residual stress computation technique. Even though the displacements due to hole drilling are small, about 0.2–0.3 pixels, and the rms noise is relatively large, about 0.1 pixels, the averaging of the large available quantity of data and the artifact compensation allowed useful residual stress measurements to be made with estimated uncertainty of about 50 MPa.

The described mathematical technique is generally applicable to full-field hole-drilling image measurements, including the ESPI, Moiré and optical DIC techniques. More accurate results are expected from optical data because of their greater measurement stability compared with SEM images. By formulating the required least-squares calculations in an efficient sequence, computation time is modest, just a fraction of a minute on a personal computer. The mathematical procedure is generally automatic with minimal human guidance required.

References

1. Lu J (ed) (1996) Handbook of measurement of residual stresses, chapter 2: hole-drilling and ring core methods. Fairmont Press, Lilburn, GA
2. Schajer GS (2010) Advances in hole-drilling residual stress measurements. Exp Mech 50(2):159–168
3. ASTM (2008) Determining residual stresses by the hole-drilling strain-gage method. ASTM Standard Test Method E837-08. American Society for Testing and Materials, West Conshohocken, PA
4. Grant PV, Lord JD, Whitehead PS (2002) The measurement of residual stresses by the incremental hole drilling technique. Measurement Good Practice Guide No.53, National Physical Laboratory, Teddington, UK
5. Makino A, Nelson D (1994) Residual stress determination by single-axis holographic interferometry and hole drilling. part i: theory. Exp Mech 34(1):66–78
6. Steinzig M, Ponslet E (2003) Residual stress measurement using the hole drilling method and laser speckle interferometry: part I. Exp Tech 27(3):43–46
7. Nicoletto G (1991) Moiré interferometry determination of residual stresses in the presence of gradients. Exp Mech 31(3):252–256
8. Wu Z, Lu J, Han B (1998) Study of residual stress distribution by a combined method of moiré interferometry and incremental hole drilling. J Appl Mech 65(No.4 Part I):837–843, Part II: 844–850
9. McGinnis MJ, Pessiki S, Turker H (2005) Application of three-dimensional digital image correlation to the core-drilling method. Exp Mech 45(4):359–367
10. Nelson DV, Makino A, Schmidt T (2006) Residual stress determination using hole drilling and 3D image correlation. Exp Mech 46(1):31–38
11. Lord JD, Penn D, Whitehead P (2008) The application of digital image correlation for measuring residual stress by incremental hole drilling. Appl Mech Mater 13–14:65–73
12. Winiarski B, Withers PJ (2010) Mapping residual stress profiles at the micron scale using FIB microhole drilling. Appl Mech Mater 24–25:267–272
13. Winiarski B, Withers PJ (2012) Micron-scale residual stress measurement by micro-hole drilling and digital image correlation. Exp Mech 52(4):417–428
14. Focht G, Schiffner K (2003) Determination of residual stresses by an optical correlative hole drilling method. Exp Mech 43(1):97–104
15. Baldi A, Bertolino F (2007) Sensitivity analysis of full field methods for residual stress measurement. Opt Lasers Eng 45(5):651–660
16. Schajer GS, Steinzig M (2005) Full-field calculation of hole-drilling residual stresses from ESPI data. Exp Mech 45(6):526–532
17. Winiarski B, Schajer GS, Withers PJ (2011) Surface decoration for improving the accuracy of displacement measurements by digital image correlation in SEM. Exp Mech. doi:10.1007/s11340-011-9568-y
18. Sutton MA, Li N, Joy DC, Reynolds AP, Li X (2007) Scanning electron microscopy for quantitative small and large deformation measurements. Part I: SEM imaging at magnifications from 200 to 10,000. Exp Mech 6(47):775–787
19. Schajer GS, Steinzig M (2010) Dual-axis hole-drilling ESPI residual stress measurements. ASME J Eng Mater Tech 132(1):71–75
20. Dahlquist G, Björk Å, Anderson N (1974) Numerical methods, chapter 4. Prentice-Hall, Englewood Cliffs
21. Sutton MA, McNeill SR, Helm JD, Chao YJ (2000) Advances in two-dimensional and three-dimensional computer vision, chapter 10. In: Rastogi PK (ed) Photomechanics. Springer, Berlin Heidelberg
22. Sutton MA (2008) Digital image correlation for shape and deformation measurements, chapter 20. In: Sharpe WN (ed) Springer handbook of experimental solid mechanics. Springer, Berlin Heidelberg
23. Pan B, Xie H-M, Xu B-Q, Dai F-L (2006) Performance of sub-pixel registration algorithms in digital image correlation. Meas Sci Technol 17(6):1615–1621
24. Tian JW, Shaw LL, Wang YD, Yokoyama Y, Liaw PK (2009) A study of the surface severe plastic deformation behaviour of a Zr-based bulk metallic glass (BMG). Intermetallics 17(11):951–957